Journal of Micromechanics and Microengineering

ACCEPTED MANUSCRIPT

A MEMS Dynamic Mechanical Analyzer for in situ Viscoelastic Characterization of 3D Printed Nanostructures

To cite this article before publication: David Cayll *et al* 2020 *J. Micromech. Microeng.* in press https://doi.org/10.1088/1361-6439/ab8bc8

JMM-104661

[1]

A MEMS Dynamic Mechanical Analyzer for *in situ* Viscoelastic Characterization of 3D Printed Nanostructures

David R. Cayll, Ian S. Ladner, Joon H. Cho, Sourabh K. Saha*, Michael A. Cullinan*

***Abstract*— Cellular, metamaterial structures with sub-micron features have shown the ability to become excellent energy absorbing materials for impact mitigation due to the enhanced mechanical properties of materials at the nanoscale. However, in order to optimize the design of these energy absorbing metamaterial structures we need to be able to measure the dynamic properties of the sub-micron features such as storage and loss moduli and the loss factor. Therefore, at scale testing is required to capture the scale, temperature, and strain rate dependent material properties of these nanoscale materials. This paper presents the design, fabrication, and calibration of a MEMS-based dynamic mechanical analyzer (DMA) that can be directly integrated with the two photon lithography (TPL) process commonly used to fabricate metamaterial structures with nanoscale features. The MEMS-based DMA consists of a chevron style thermal actuator used to generate a tensile load on the structure and two differential capacitive sensors on each side of the structure used to measure load and displacement. This design demonstrated 1.5 ± 0.75 nm displacement resolution and 104 ± 52 nN load resolution, respectively. Dynamic mechanical analysis was successfully conducted on a single nanowire feature printed between the load and displacement stages of the MEMS device with testing frequencies ranging between 0.01 – 10 Hz and testing temperatures ranging between 22°C - 47°C. These initial tests on an exemplar TPL part demonstrate that the printed nanowire behaves as a viscoelastic material wherein the transition from glassy to viscous behavior has already set in at the room temperature.**

***Index Terms*—Two Photon Lithography, Direct Laser Writing, Microscale Dynamic Mechanical Analyzer, Dynamic Mechanical Analysis**

[1]Manuscript Submitted March 24, 2020. This work was supported by the U.S. Department of Energy by Lawrence Livermore National Laboratory under Contract DE-AC52-07NA27344 and by the University of Texas at Austin under Subcontracts. Funding was available from LLNL's LDRD project 16-ERD-047

Authors D. R. Cayll, J. H. Cho, and M. A. Cullinan are with the University of Texas at Austin, Austin, TX 78712 USA. (email: Michael.cullinan@austin.utexas.edu)

I.S. Ladner was with the University of Texas at Austin, Austin, TX 78712 USA. He is now with Lawrence Livermore National Laboratory, Livermore, CA 94550 USA.

S. K. Saha was with Lawrence Livermore National Laboratory, Livermore, CA 94550. He is now with Georgia Institute of Technology, Atlanta, GA 30332 USA. (email: sourabh.saha@me.gatech.edu)

I. Introduction

Recent developments in additive manufacturing have enabled the fabrication of cellular metamaterials with complex architectures and feature sizes down to the nanometer scale [1], [2]. These advances have made it possible to produce materials with exceptional mechanical properties [3]. This is because when the individual features in a cellular material become nanoscale in size they can exhibit a "size-effect" where the materials show improved mechanical properties such as increased strength as compared to its bulk properties. For example, mechanical metamaterials with sub-micron features have been developed that have shown great promise for absorbing the mechanical energy of an impact as compared to the existing technologies [4]. The impact mitigation ability of these materials could lead to significant advances in sensor packaging for use in extreme environments. The bulk materials that are used to form these metamaterial structures are known to be viscoelastic and thus have strain rate dependent mechanical properties which are critical for high strain rate applications such as impact. However, size-dependent viscoelastic properties of these nanoscale features within metamaterial structure are not well known due to the lack of reliable, in situ methods for measuring the dynamic properties of materials at the nanoscale. Therefore, the purpose of this paper is to present the design, fabrication, and calibration of a MEMS-based dynamic mechanical analyzer that can be used to make direct measurements of the viscoelastic properties of nanoscale structures.

Dynamic Mechanical Analysis (DMA) is the method through which viscoelastic properties such as loss modulus, storage modulus, and damping factor are measured. There are a number of different ways to measure these properties which can include axial, torsional, stress controlled, and strain controlled testing methods[5]. The choice of the method depends on the sample geometry, the desired accuracy, and the material type. Regardless of the tool chosen, all DMA tests collect time varying stress and strain response of a material deforming under an oscillating load. The phase difference between the oscillating stress and strain is directly related to the internal damping in the material, and this phase difference is an important measure of the viscoelasticity of the material [5]. For an accurate measurement of the viscoelastic properties of nanoscale structures, one must implement a dynamic testing system that is on a scale similar to the parts it will be testing. Here, we have used two-photon lithography (TPL) to fabricate nanoscale features and designed a MEMS-based DMA on the same scale as the fabricated features to perform the viscoelastic measurements.

TPL is an additive manufacturing (AM) method capable of writing millimeter-scale complex three-dimensional (3D) structures with sub-micron features. Sub-micron features smaller than the diffraction-limited light spot can be achieved in TPL due to the non-linear nature of the two-photon absorption process. During TPL, a focused light spot

polymerizes a single volumetric pixel, or voxel, within a photosensitive medium [6]. Researchers have taken advantage of the sub-diffraction resolution of TPL in applications including photonics [7], nano/microstructures [1], [8], [9], high density physics [10], and bioengineering [11], [12]. With the emergence of refractive index matching protocols for new TPL materials [13] and continuing work on parallel writing systems [14], the polymers and the writing process parameters in TPL are constantly evolving. In order to deterministically design metamaterials using TPL, the printed nanoscale voxels must be characterized at scale.

Despite the need for at-scale DMA tests, the most common current method for analyzing the dynamic mechanical properties of TPL materials is compression of lattice structures with a macro-scale nanoindenter[15], [16]. In these studies, time variant load and displacement data are collected by the nanoindenter and used to calculate the real and complex moduli or stress relaxation times. Due to the millimeter scale of the nanoindenter tips, this method characterizes the structural response of the metamaterials instead of the material response of the nanoscale features. Estimation of the material response from the structural response necessitates making several assumptions that may not be physically accurate. For example, the method assumes that the Poisson's ratio is fixed at the bulk value even with nanoscale feature sizes [17]. Attempts have been made to eliminate this assumption by using bending of cantilevers as an alternate loading mechanism [17], [18]. However, this approach is also limited to capturing only the structural properties.

There has also been work done using MEMS based nanoindenter technology such as the commercially available FemtoTools™ setup[19]. MEMS based indenters have the advantage of small tips and high load and displacement resolution, but commercially available tools cannot easily be used in situ for TPL polymer testing without an integration step such as pick and place with FIB deposition clamping[20]. There has been some work with using contact-resonance AFM for viscoelasticity (CRAVE) to measure complex modulus, but many assumptions need to be made such as tip geometry, contact model, Poisson's ratio, and the modulus of calibration material [21]. CRAVE is also limited to testing at the frequency at which the AFM cantilever beam resonates at.

Microelectromechanical system (MEMS) tensile testers with integrated sensing are an attractive solution for characterization of nano and micro scale structures due to the nN force resolution and mN force range. Several designs have been produced to study thin films [22], [23], nanotubes and wires [24]–[27], and polymeric nanofibers [28]. Traditionally, specimens are synthesized on one substrate and moved to the tensile tester using a pick and place approach. However, pick-and-place methods can damage the soft polymer materials typically used in energy absorbing metamaterial structures. With TPL being an AM process, researchers can fabricate specimens directly onto the tensile tester. In 2018, Jayne et al. demonstrated this capability by printing a negative Poisson's ratio bowtie structure between a fixed stage and an actuator [29].

In this paper, we continue the process integration between TPL and MEMS by developing a process compatible MEMS dynamic tensile test system to conduct *in situ* dynamic mechanical characterization. This approach enables TPL material characterization in the scale, frequency, and temperature dependent regime independent of structure and structural characterization under tensile loading. The measurement bandwidth is wider than AFM based measurements, but lower than piezo driven nanoindenter tools. However, MEMS actuators will allow for purely tensile load unlike both AFM and indenter measurements. Designing a MEMS device for process integration differs from previous work due to the in-use exposure to sources of stiction. All mechanically suspended structures are designed to withstand both vertical and lateral sources of stiction during TPL.

II. Device Design and Fabrication

A. Device Design

The MEMS DMA presented consists of a thermal actuator and differential capacitive load and displacement sensors, shown in Figure 1 and 2. Chevron style thermal actuator

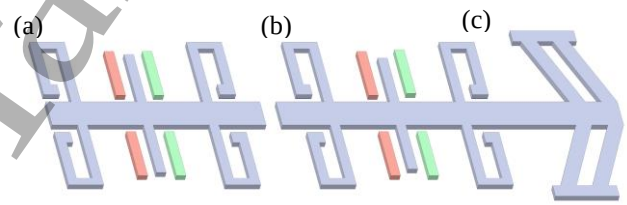

Figure 1(a) Load sensor (b) displacement sensor (c) thermal actuator

generates displacement-controlled tensile loads along the central shuttle that are ideal for strain-rate dependent testing [10], [25]. The load and displacement sensors are surface micromachined differential capacitive displacement sensors which are used to measure the specimen elongation and the stretching force. Both sensors are suspended by double parallelogram flexure bearings connected to their respective shuttles, which limits the out-of-plane motion during testing and provides the stiffness for the load sensor. The central shuttle of the displacement sensor is directly connected to the thermal actuator. This style of mechanical tester has been demonstrated for a variety of materials such as carbon nanotubes [24], crystalline nanowires [30], polymer nanofibers [31], and a variety of testing conditions such as quasi-static tensile testing [32], tensile fatigue testing[23], and dynamic testing [33]. Dynamic testing with this design is limited to low frequencies (< 1 kHz) because of the time required to heat and cool the beams, or thermal time constant [34]. Fortunately, this type of response time is adequate for dynamic mechanical analysis of photopolymers used in TPL where test frequencies above 0.1 Hz remove the effects of creep and strain relaxation, and through Boltzmann's superposition principle, higher frequency data can be found through increased temperature testing[5].

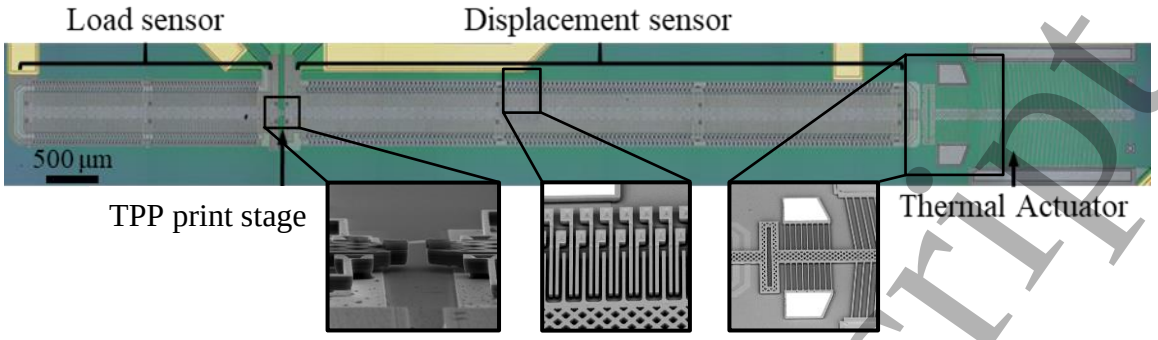

Figure 2. As fabricated, custom MEMS dynamic mechanical analyzer (DMA)

The actuator dimensions were chosen in order to keep a large displacement range of up to 1.5 µm so that fatigue and quasi-static tensile tests could also be performed with this test setup. This design choice gives the MEMS-based DMA a lot of flexibility in the types of measurements that it can make, but there is an inherent tradeoff between overall displacement, force, and working frequency. If the displacement range requirement was removed from the device design, then the actuator could be optimized to function with a larger bandwidth. In addition, the Boltzman superposition principle states that there is a time and temperature relationship that allows for the expansion of DMA data in the frequency domain by changing the temperature of tests[5]. Therefore, the MEMS-DMA setup was designed with a temperature control system to allow the nanomaterials to be tested over a wider effective range of use cases. To control temperature, a heat path was created between the MEMS DMA device and BriskHeat® heating tape used as our heat source. Figures 4a & b displays the heat path along with an image of the final measurement setup.

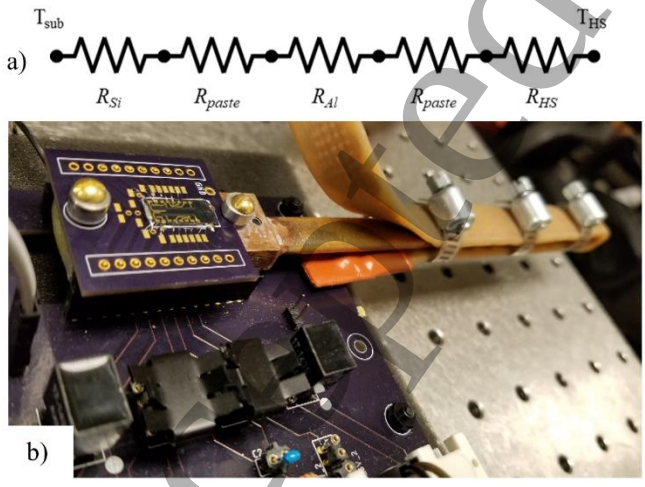

Figure 3 (a) Lumped thermal model, (b) thermal management system

One of the other major challenges for performing any mechanical analysis on submicron scale polymer materials, such as single voxel TPL lines, is preventing damage or defects during sample handling. In the subsequent sections, this design includes stiction analysis to integrate the MEMS tensile tester into the TPL writing process and remove sample handling yield problems.

B. *In- and Out-of-plane Stiction*

Stiction is a failure method common in MEMS where suspended mechanical elements permanently deform and adhere to another surface due to interfacial forces [35]. Due to pick and place transfer methods, MEMS tensile testers predominantly encountered stiction during wet release of sacrificial layers. With modifications to the fabrication process, such as critical point drying [24] or vapor hydrofluoric acid (HF) release [23], stiction due to capillary forces can be avoided. However, integration of the TPL and MEMS process exposes device features to capillary forces during writing and development, and potentially surface-to-surface adhesion during the writing phrase.

Process integration of TPL and MEMS is illustrated in Figure 4 where a droplet of a photopolymer resist is dispensed near the ends of the load and displacement sensor shuttles of the device, and the device is loaded into the TPL system. Then, an objective is raised into contact with the resist droplet

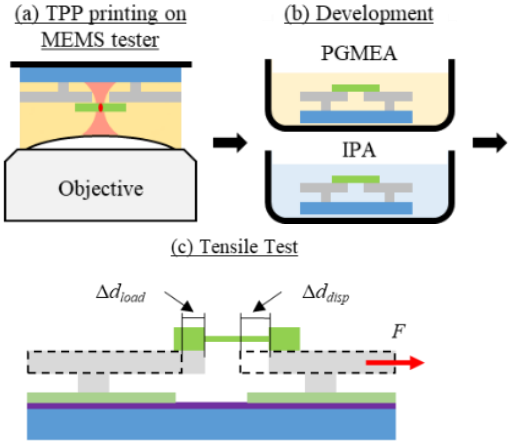

Figure 4. Schematic of the process integration of a MEMS tensile tester with TPL.

and a galvanometer stage guides the laser to write the tensile specimen. After writing is complete, the device is placed into propylene glycol monomethyl ether acetate (PGMEA) development solution to remove the non-polymerized resist followed by cleaning with isopropyl alcohol (IPA). Finally, the device is dried in air to release it for dynamic mechanical

analysis. Consequently, the MEMS DMA is exposed to in- and out-of-plane capillary forces and potentially surface contact adhesion requiring stiction resistance design. Figure 5 illustrates the out-of-plane stiction failure modes potentially

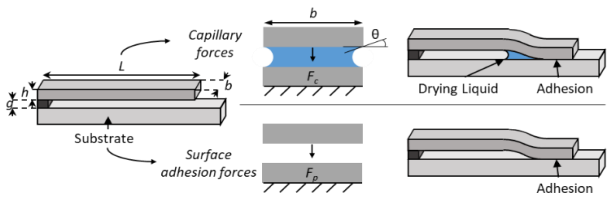

Figure 5. Illustration of the two dominant stiction modes with capillary on top and surface adhesion on bottom.

present during fabrication.

Mastrangelo and Hsu [36] developed the characteristic stiction equations for capillary, or elastocapillary, and surface-to-surface, or peel, failure. The equations balance the elastic energy of the suspended geometry versus the interfacial forces with a characteristic number. The elastocapillary number, N_{EC}, and peel number, N_p, for the fixed-free vertical case, are

$$N_{EC} = \frac{2Eg^2h^3}{9\gamma_l cos\cos\theta_c L^4\left(1+\frac{h}{b}\right)} \quad (1)$$

$$N_P = \frac{3Eg^2h^3}{8\gamma_s L^4} \quad (2)$$

where E is the elastic modulus, g the gap between the base of the suspended beam and the substrate, h the beam height, L the beam length, b the beam width, γ_l the liquid surface tension, θ_c the liquid contact angle, and γ_s the solid surface tension. For in-plane analysis, g is replaced with the smallest gap between the capacitor fingers, and h and b are interchanged [37]. For both numbers, if $N > 1$ the beam will remain suspended, and if $N < 1$ the beam will be pinned to the surface. When $N = 1$, L is the critical length, L_c, where stiction will occur.

For our operating conditions, the liquid parameters γ_l and θ_c are 21.7×10^{-3} N/m^{-1} and 0° respectively for IPA, the final liquid in the process (Figure 5). γ_s is 165×10^{-3} N/m^{-1} for the surface adhesion between polysilicon surfaces. Correction factors of 2.9 for elastocapillary and 2.5 for peel are applied to L_c for fixed-fixed boundary conditions. Due to the total length of the sensors, anti-stiction dimples, or hemispherical structures, are placed along the central shuttle at 60 µm interval to reduce the contact area [38]. Safety factors of 1.5 were added to account for potential variations in dimensions and surface conditions.

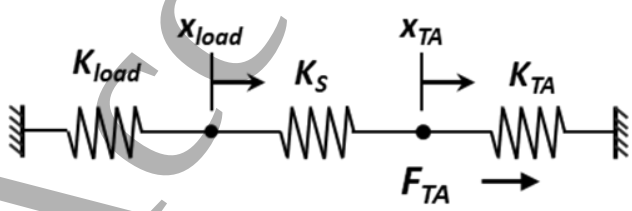

Figure 6. Lumped mechanical model

In-plane stiction and electrostatic pull-in, i.e. when the electrostatic force is high enough to pull the capacitive fingers together, were also considered during the design of the differential capacitors due to the small gap sizes between the capacitor fingers [39]

C. Mechanical Analysis

1) Lumped Mechanical Model

When the nanoscale rod feature is printed between the two sensors, it forms a single, serial mechanical system which can be modeled through a combination of springs as illustrated in Figure 6. Displacement and force balance equations were derived from the lumped model to design the thermal actuator to meet the force and displacement requirements. The equations are

$$x_{load} + x_s = x_{TA} \quad (3)$$

$$K_{load}x_{load} = K_s x_s \quad (4)$$

$$K_s x_s + K_{TA}x_{TA} = F_{TA} \quad (5)$$

where x and K is the displacement and stiffness for the load sensor, *load*, specimen, *s*, and thermal actuator, *TA*, respectively. F_{TA} is the force produced by the thermal actuator. As seen in Eqs. (4) and (5), an estimate of the K_s is required in order to complete the mechanical design. K_s was estimated to be ~140 N/m for this design based on the size of the printed features and the elastic modulus of the material from literature [40].

Table 1. Design goals for load and displacement sensors

Parameters	Resolution	Maximum
Force	75 nN	250 µm
Displacement	0.625 nm	1.5 µm
Structure Stiffness	~140 N/m	

With a polymeric test specimen, displacement control is critical in order to perform the dynamic mechanical analysis correctly. To achieve this, the design of the thermal actuator is done in the loaded conditions, represented by Eq. (5). In the load condition, both the specimen and thermal actuator itself provide a resistive force. Solving Eq. (5) at F_{TA} = 0 and substituting with Equation (4), x_{TA} can be written as a ratio of stiffnesses

$$x_{TA} = -\frac{K_s x_s}{K_{TA}} = -\frac{K_{load}x_{load}}{K_{TA}} \quad (6)$$

The impact on x_{TA} by x_s or x_{load} can be reduced to ≤1% by designing K_{TA} to be ≥ 100 times the sum of K_s and K_{load}. The exact ratio has to be balanced with other design requirements, such as the 15% desired strain.

2) Load Sensor

The load sensor shuttle is suspended by a double parallelogram flexure bearing which converts the sensor's displacement into force. This flexure bearing design limits out-of-plane motion to the nanometer range which is critical

for maintaining uniaxial loading with submicron features. The stiffness bounds for K_{load} are set by the tradeoff between the desired range and resolution of the device. The maximum stiffness that could be used to still achieve the desired range is set by the maximum force on the specimen, 250 µN, divided by the maximum desired specimen elongation x_s = 1.5 µm for quasi-static tensile tests. The minimum stiffness that could be used to still achieve the desired resolution is set by the desired force resolution, ≤ 35 nN, divided by the displacement resolution of the differential capacitive sensor, Δd. (Δd for the load sensor is 0.25 nm, which has been previously demonstrated for this style of capacitive sensor [24]). The resulting stiffness bounds are 140 N/m to 166.7 N/m. Therefore, K_{load} was chosen to be 150 N/m for this design. The exact beam geometries of the flexure bearings were also selected to have N_{EC} and $N_P \geq 1.5$ to prevent out-of-plane stiction.

3) Thermal Actuator

A chevron style thermal actuator was selected for its high maximum force and displacement-controlled actuation. To achieve more than 1.5 µm of elongation (15% strain of a 10 µm specimen), the design focused on balancing the stiffness and force to satisfy (3). The stiffness is

$$K_{TA} = 2N_{TA}\left(sin^2\theta\,\frac{Eb_{TA}h}{L_{TA}} + cos^2\theta\,\frac{Eb_{TA}^3h}{L_{TA}^3}\right) + K_{HS} + K_{disp} \quad (7)$$

where N_{TA} is number of beam pairs, E the Elastic modulus of polysilicon, b_{TA} the beam width, h the beam thickness, L_{TA} the beam length, and θ the incline angle of the beams. K_{HS} and K_{disp} are the stiffnesses of the fixed-guided heat sink beams and displacement sensor flexure bearings, respectively. Heat sink beams were sized to reduce the temperature at the specimen end of the central shuttle. Flexure bearings for the displacement sensor were designed to support the shuttle.

Force generated by the thermal actuator, F_{TA}, is

$$F_{TA} = 2N_{TA}EA\alpha\Delta T\sin\theta \quad (8)$$

where A is the beam cross sectional area, α the coefficient of thermal expansion for polysilicon, and ΔT the average temperature change of the beam. To prevent recrystallization of the polysilicon during operation, maximum ΔT was set to 525°C [41].

From Eqs. (4) and (5), three variables were selected to balance displacement and load: N_{TA}, L_{TA}, and b_{TA}. h *is* 8 µm to meet out-of-plane stiction requirements for the capacitor fingers, and θ is 6° to approach maximum displacement without introducing buckling [42]. N_{TA}, L_{TA}, and b_{TA} were determined using Eqs. (3) – (8) to reach x_{load} *and* x_s without buckling or pinning.

Eq. (3) can be rewritten with F_{TA} divided by K_{TA} in place of x_{TA} to produce an equation for displacement independent of N_{TA}. The upper bounds for b_{TA} is set by the unloaded critical buckling load, and the lower bound is set to 8 µm to fix buckling failure in the normal direction. Since the critical buckling load occurs between the unloaded and loaded condition [42], a minimum safety factor of 2 was applied. The upper limit for L_{TA} is set by the critical length of the peel number, which dominates the out-of-plane failure method, under a square plate boundary condition. Once values for b_{TA} and L_{TA} achieved the desired displacement, N_{TA} was tuned to satisfy Eq. (8) while limiting the footprint of the thermal actuator.

The design resulted in a thermal actuator with 30 sets of 320 µm long, 8 µm wide, and 8 µm thick beams at an incline angle of 6°. K_{TA} is 27.2 kN/m, which results in an actuator to specimen plus load sensor stiffness ratio of 94. The maximum F_{TA} is 265 µN.

D. Sensor Design

Surface micromanufacturing style differential capacitors were selected for high sensitivity and compact footprint [16]. Figure 7 is a schematic of a single differential capacitor unit used in this design. Change in capacitance ΔC as the central shuttle moves is

$$\Delta C = 2n\varepsilon l_o h\frac{1+2\left(\frac{C_3}{C_0}\right)}{d_0^2}\Delta d \quad (9)$$

where n is number of differential capacitor unit cells, ε is relative permittivity, l_0 is overlap length between the stationary finger (blue and orange fingers in Figure 7) and moving finger (grey finger in Figure 7), h is finger thickness, C_3 is capacitance between the stationary fingers, C_0 is capacitance between the stationary and moving fingers at the initial position, d_0 is initial gap between stationary and moving fingers, and Δd is change in displacement of the moving finger. ΔC was set to 0.1 fF for all sensors, which is double the previously demonstrated noise floor [24]. Δd was set to 0.25 nm for both the load and displacement sensors

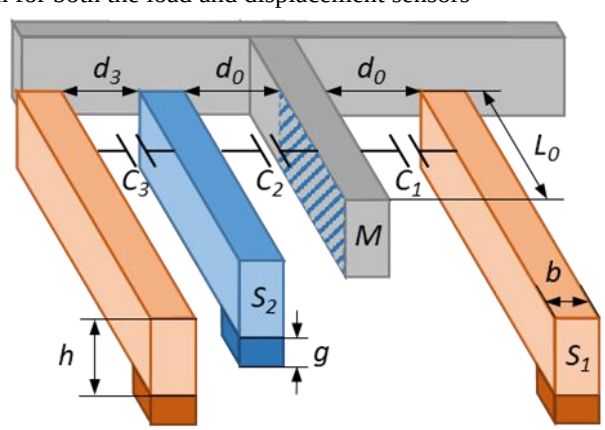

Figure 7. Schematic of differential capacitor with labels. The blue gradient pattern on the M beam represents the initial overlap area, A1.

The values for d_0 were chosen to be at least 0.5 µm greater than x_{load} and x_{TA} plus the displacement due to pull-in voltage for the load and displacement sensor respectively. The remainder of the unit cell design was done to reduce stiction. First, the l_0 was limited by vertical peel number of the exterior stationary finger (Figure 7). With h = 8 µm and g = 2.5 µm plus the required clearances for the fabrication, the maximum

l_o was 83 µm with an N_p = *1.5*. In-plane stiction was used to design the finger width, *b*, and the spacing between the stationary fingers, d_3, which are terms in C_0 and C_3 respectively. *b* and d_3 were selected to increase the capacitance of a unit cell while maintaining N_{EC} and $N_P \geq 1.5$. Once the unit cell was sized, *n* was increased until $\Delta C = 0.1$ *fF*.

With l_0 limited by stiction, *n* increased into the hundreds of unit cells results in millimeter range shuttles. To account for the increase in shuttle length, additional flexure bearings were evenly distributed along the length of the shuttle to limit sag and to help prevent stiction. This required resizing the flexures to maintain the desired stiffness values for K_{load}. Changes to K_{disp} were acceptable as long as Eq. (5) was still satisfied. Even with the extra flexures, some sections of the shuttle were not reaching N_{EC} or $N_P > 1$. To further improve stiction resistance, dimples were added on both sides of the shuttle to reduce the contact surface area. The dimples were place every 60 µm resulting in N_{EC} or $N_P > 5$.

A full schematic of the tester circuit is shown in Figure 8. A charge integration circuit was implemented to measure the differential capacitive sensors. This circuit uses an Analog

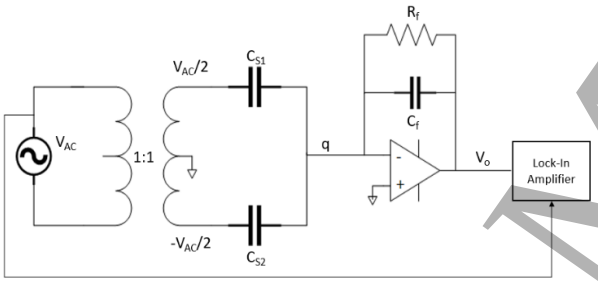

Figure 8. Charge integrator capacitance measurement circuit

Devices LT1793 op-amp with ultra-low noise and high input impedance as a charge integrator. The Zurich Instruments UHF lock-in amplifier (LIA) with built-in digital signal processing and logging capabilities was used to measure the magnitude of output voltage, V_O, at the reference frequency V_{AC}. Using the lock-in amplifier for this measurement demodulates the output signal and passes it through a low pass filter so the signal at frequency f_{AC} is sufficiently low noise. Equation (10) and (11) describe the relationship between charge, change in capacitance, and output voltage in the circuit in Figure 8

$$q = \frac{1}{2}(C_1 - C_2)V_{AC} \tag{10}$$

$$V_O = \frac{1}{C_f} q \tag{11}$$

Charge accumulated on the common terminal, 'M' in Figure 7, of the capacitors C_1 and C_2, is directly proportional to the magnitude of change in capacitance between the two capacitors. The frequency of V_{AC} was set at 500 kHz to stay below the bandwidth of the op-amp. C_f was minimized to maximize the gain of the amplifier, and R_f was used to tune the cutoff frequency of the amplifier. In order to reduce noise further, a low pass filter was implemented that utilized the digital processing capabilities of the UHF LIA. This filter was used to filter the V_O signal so that a sine wave could be fit in the time domain to extract the valuable phase information from the DMA tests.

E. *Fabrication*

The process flow shown in Figure 9(a-f) is a cross section view of a two polysilicon layer PolyMUMPs process [43]. Polysilicon 1 is the base electrical layer, and Polysilicon 2 is the device layer. Both layers are deposited as amorphous silicon and doped/annealed with spin on phosphosilicate glass (PSG). Polysilicon 2 was deposited in 1 µm layers with PSG doping every two layers. This modification to the PolyMUMPs process flow was due to a limit on the LPCVD amorphous silicon tube furnace. A second modification was the 300 nm Au/Cr metallization bi-layer liftoff step prior to

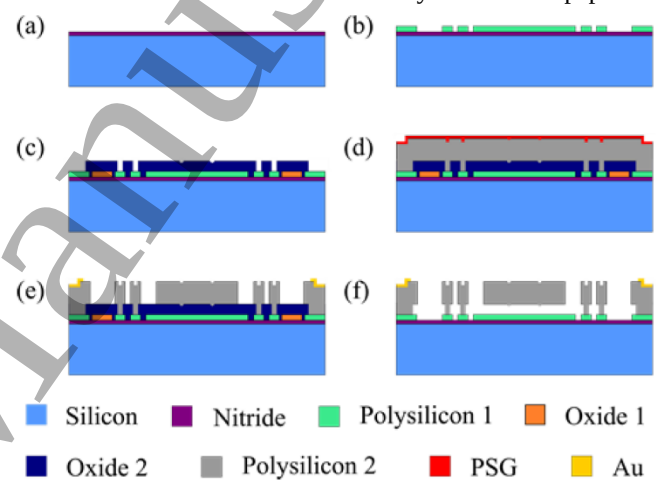

Figure 9. Fabrication process flow

patterning the Polysilicon 2 layer. This approach provided a less turbulent surface for bi-layer liftoff process. Deep reactive ion etching (DRIE) was used to etch the 8 µm Polysilicon 2 layer.

At this point, wafers were diced into chips. The chips were cleaned in Nanostrip® solution followed by acetone and IPA prior to a BOE wet etch to remove the sacrificial oxide, Oxide 1 and 2. After etching was complete, the chips were placed in a DI water, IPA bath, and dried in air. An image of the final fabricated device is shown in Figure 2.

III. Calibration

Calibration of the testers measured the performance of the thermal actuator, displacement sensor, and the load sensor. Due to the structure, the thermal actuator and displacement sensor were calibrated together as the displacement sensing unit. A similar tester was designed with the two stages rigidly bonded together for calibration of the load sensor.

A. *Displacement Sensing*

A stepwise dc actuator signal was applied and recorded while capturing the physical displacement of the capacitive fingers using the Keyence VK-X250 Laser microscope with a 100x

lens and Super High-resolution mode. Digital image correlation (DIC) in NI Vision was used to measure the displacement between diamond shaped etchant access holes on the displacement shuttle and the fixed points of the flexure

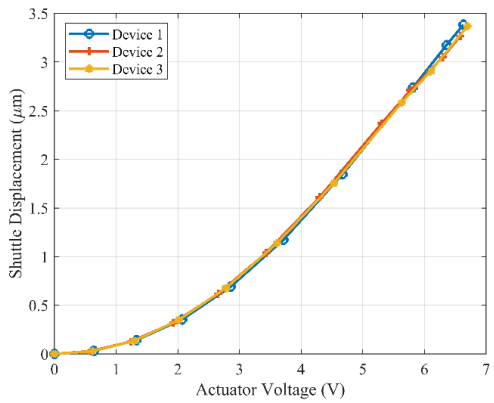

Figure 10. Thermal actuator displacement calibration curve

bearings. In this approach, any drift from the microscope stage was minimized by measuring two fixed points on the device itself and resulted in a DIC error of 1.8 nm. Figure 10 shows the measured calibration curve for three different devices. Results show good repeatability between devices.

$$d = \left(\frac{V}{3.49}\right)^2 \tag{12}$$

The MEMS DMA was designed as a strain-controlled device; therefore, the force imparted by the load stage will not affect the location of the displacement stage. This allows the location of the displacement stage to be found deterministically using Eq. (12) that calibrates the voltage applied across the thermal actuator to the displacement of the actuator.

Since the dynamic tests are only run up to 10 Hz where the time delay from heating the thermal actuator beams is negligible, as shown in Figure 14, Equation (12) can be used to deterministically locate the displacement stage. Uncertainty in the constant in the denominator is 0.025 $V/\sqrt{nm}$, or 1.4 nm at a full 100 nm actuation.

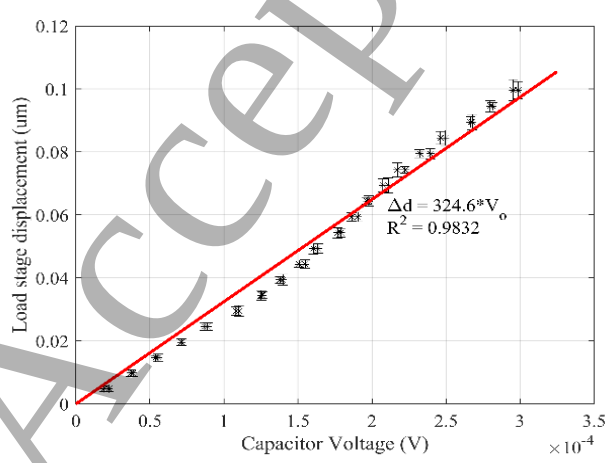

Figure 11. LIA charge integrator output calibration curve

B. *Load Sensing*

Both the displacement and stiffness calibration are required for an accurate measurement by the load sensor. To calibrate the load side of the stage, a chip with a rigid connection between the displacement sensor and load sensor was fabricated and tested. Figure 11 shows the linear response between actuated distance and LIA circuit output voltage. Since this system will always be actuated with a sine wave, the sensor was calibrated with a sine wave. The amplitude of actuation voltage was determined using Eq (12), and 15 periods of response were recorded. This data was then curve fit, and the error bars shown in Figure 11 are the standard deviation of amplitude. The standard deviation of the position averaged across the full range is 1.5 nm. This translates into a load resolution of 104±52 nN, where the uncertainty is error in load cell stiffness and displacement error combined.

The curve fit method was used over FFT because the error is more easily quantifiable and data fidelity can be found using the coefficient of determination, R^2. An example of this curve fit of the connected stage calibration device at 50 nm of displacement and 0.1 Hz is shown in Figure 12.

The last part of the load cell that must be characterized is the stiffness of the linear flexures. These provide the restoring force that will allow us to measure the force on the printed nanoscale feature between the stages.

Stiffness of the load sensor flexure bearings was calculated for each device by running a finite element analysis (FEA) with updated beam geometries from SEM measurements of the fabricated devices and including a sidewall angle. This method has been shown to be within ± 2.5% of experimental results [42]. The standard deviation of beam geometries across the chips in this study are ± 1.07 µm for length, ± 0.54 µm for width, and ± 0.05 µm for height, and the sidewall angle produced by DRIE ranged from 2° - 9.5°. The estimated average stiffness values across the chips is 105 ± 33 N/m, which includes a 5% deviation in Elastic modulus [42]. While the large geometry variations traditionally limit the acceptable devices, it allowed for the selection of tensile testers with load cells stiffnesses closer to stiffness of the test structures. The load cell stiffness for this study was 69.44 ± 3.82 N/m

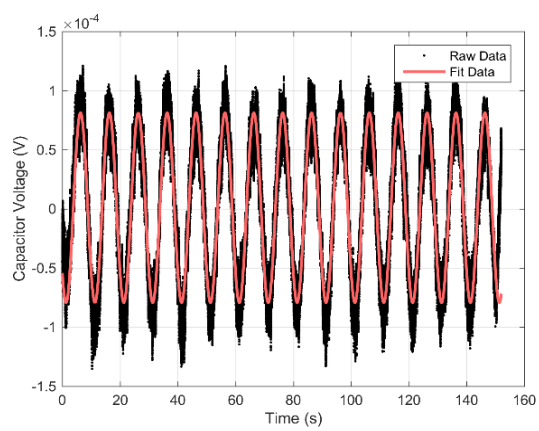

Figure 12. Load stage capacitive sensor voltage output, Vo, and raw sensor data with best fit line vs Time. RMSE = 1.65e-5; R^2 = 0.919

C. *Operating frequency range*

The actuator settling time can be found using an analytical model based on geometry and material properties presented by Hickey et. al. [34]. The thermal actuator as designed in this study, has a thermal settling time of 791 µs. This means after time τ, the output has reached 63% of its final value. This is confirmed by a dynamic simulation. Figure 14 shows the transient response of the actuator to a representative sine wave at 3 different frequencies: 10, 100, and 1000 Hz. This figure shows that there is virtually no lag in the actuator response at the 10 Hz frequency, but that actuator lag can become significant at higher frequencies. Therefore, in order to ensure fidelity of the time response of the thermal actuator, dynamic tests should be limited to 10 Hz for this study. However, previous dynamic mechanical analysis studies have shown that similar polymeric materials exhibit viscoelastic behavior in the range of 0.1 - 10 Hz [19].

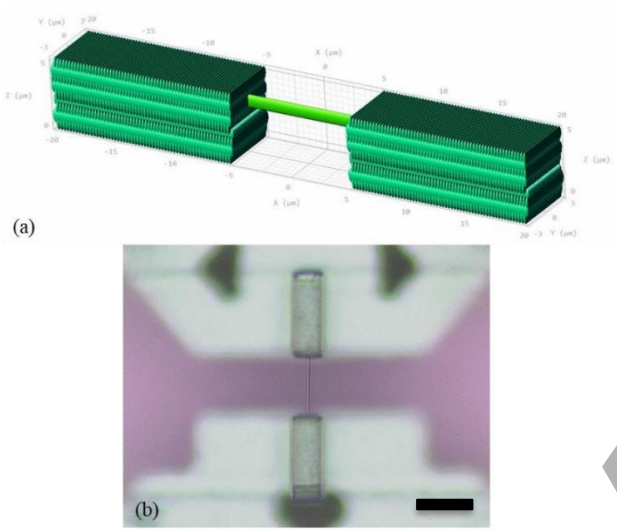

Figure 13. (a) Isometric view in DeScribe and (b) top view optical image of tensile part. Scale bar is 10 µm

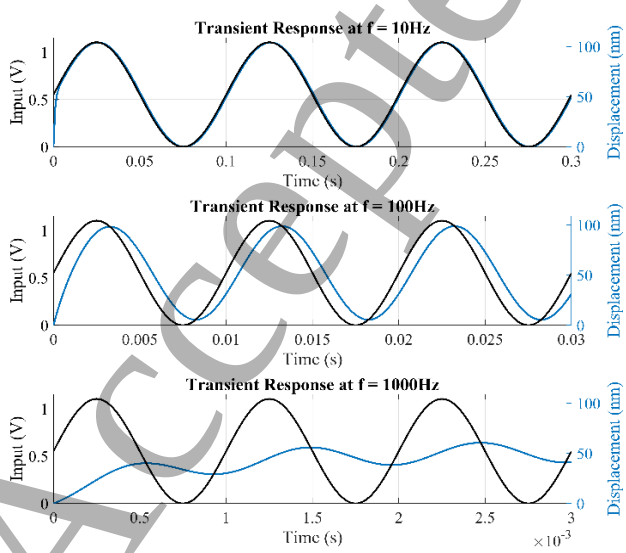

Figure 14. Transient response of as designed thermal actuator at (a) 10 Hz, (b) 100 Hz, and (c) 1000 Hz

IV. Experimental Results and Discussion

A. *TPL Time and Temperature Tests*

Figure 13(a) shows a CAD rendering and printed test structure of a single voxel nanowire feature suspended between contact pads on each sensor. The contact pad sizes were chosen to be 40x larger than the structure cross-sectional area to prevent adhesion failure prior to elastic yielding. All structures were printed on the Nanoscribe system with IP-Dip photoresist at 40 mW average power and 10 mm/s speed which produces oval voxel lines 285 ± 8 nm wide and 0.95 ± 0.02 µm tall [32].

During testing, a sinusoidal displacement is used to drive the thermal actuator, so the relation in Eq. 9 was used to find the corresponding voltage signal. A maximum displacement of 100 nm, or 0.1% strain, was chosen so that the printed nanowire would stay in the viscoelastic regime [44]. Stress, strain, and phase delay data (δ) were collected, and using Eq. (13) – (15), storage modulus, loss modulus, and loss factor, respectively, were calculated.

$$E' = \frac{\sigma_0}{\varepsilon_0} cos\delta \quad (13)$$

$$E'' = \frac{\sigma_0}{\varepsilon_0} sin\delta \quad (14)$$

$$tan\delta = \frac{E''}{E'} \quad (15)$$

The frequency range of the tests of 0.01-10 Hz was chosen because of the tradeoff between data collection time, temperature stability, and data collection range. 0.01-10 Hz is also a very typical frequency test range for macroscale DMA tests. The temperature range of 21.5°C - 47°C was chosen to

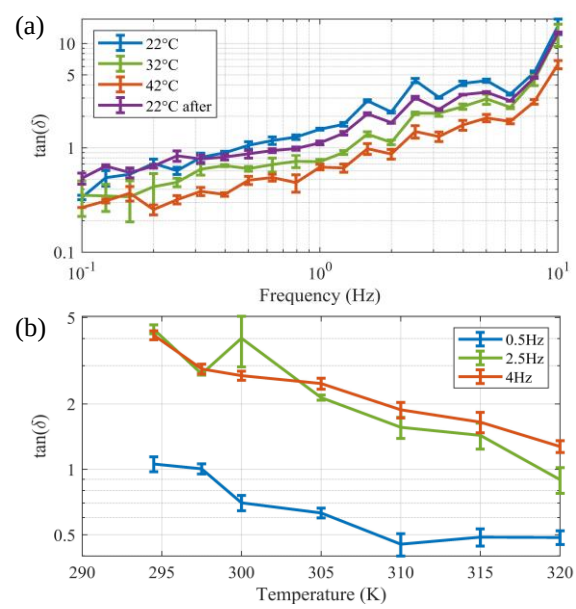

Figure 15. (a) Loss factor vs. frequency of TPL printed part at 3 different temperatures. (b) Loss factor as a function of temperature for 3 separate drive frequencies.

stay below the quoted degradation temperature of the IP-Dip material [40]. In order to control temperature, resistive heating tape was connected to the heat sink that was thermally connected to the MEMS tensile tester as described by Ladner et. al [45]. The device was then monitored in real time under an FLIR a655sc thermal camera. This setup was thermally stable to within $\pm$ 1°C.

Initial results from a time-temperature scan of a single printed nanowire are presented in Figure 15 (a) and (b) which show the loss factor, tan(δ), as a function of frequency and temperature, respectively. The figures show that as frequency increases, so does tan(δ), and as temperature increases, tan(δ) decreases.

Figure 16 (a) and (b) present the measured real component of the elastic modulus of the nanostructures fabricated by TPL with the IP-Dip material verses frequency and temperature, respectively. As frequency and temperature increase, the storage modulus generally increases, which indicates an increase in rigidity. Figure 17 (a) and (b) show the corresponding complex component of elastic modulus, or loss modulus. With increasing frequencies, the loss modulus increases, but there seems to be little change with temperature. Discussion on these results are in the following section.

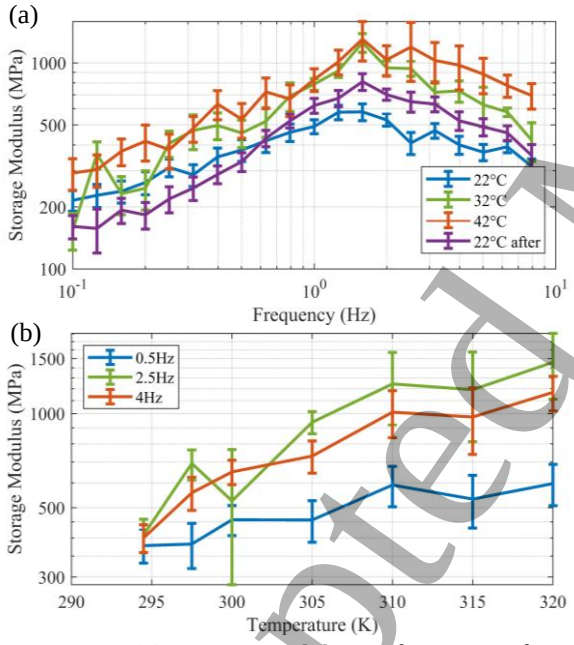

Figure 16. (a) Storage Modulus vs. frequency of TPL printed part at 3 different temperatures. (b) Storage Modulus vs. temperature for 3 separate drive frequencies.

B. Discussion

In dynamic testing of viscoelastic materials, two quantities are typically measured, the storage modulus (E') and the loss modulus (E''). The storage modulus measures the energy stored by the material during deformation and thus is a measure of elastic response of the material. The loss modulus measures the energy dissipated during deformation and thus is a good measure of viscous response of the material. Tan(δ) is the ratio of loss to the storage and is a measure of the damping in the material.

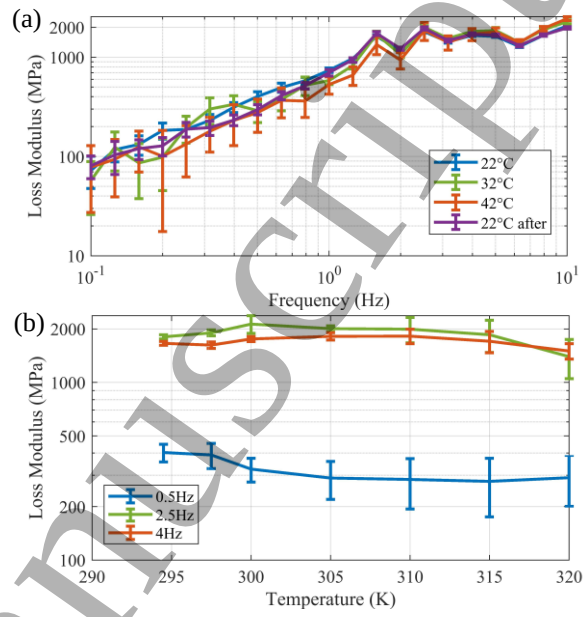

Figure 17. (a) Loss Modulus vs. frequency of TPL printed part at 3 different temperatures (b) Loss Modulus vs. temperature for 3 separate drive frequencies.

Generally, as a polymer is heated and it nears the glass transition temperature, there is a large peak in the loss modulus [46] which corresponds to a drop in mechanical strength or storage modulus. An example of typical polymer behavior is presented in Figure 18(a). In general, the loss modulus is lower than the storage modulus before and after the glass transition temperature but may exceed the storage modulus in the transition region. Comparison of the experimental results with the typical response curves for polymers suggests that the printed nanowire feature lies at the end of the glass transition regime as highlighted in Figure 18.

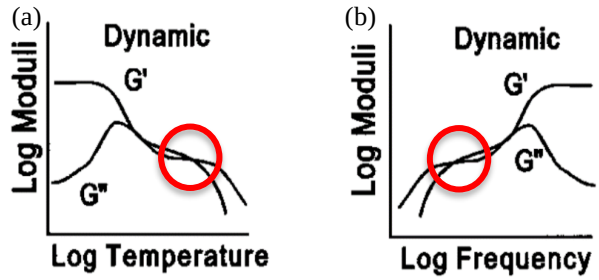

Figure 18. Typical real modulus, G', and complex modulus, G'', curves for polymers. From: Dynamic Mechanical Analysis: A Practical Introduction, *K. P. Menard, Copyright 1999. Reproduced by permission of Taylor & Francis Group.[5]*

This is supported by the following observations: (i) the loss modulus exceeds the storage modulus at higher frequencies but not at lower frequencies, (ii) the loss modulus monotonically increases with increasing frequency, and (iii) the storage modulus has a peak value at a moderate frequency

(~ 1 Hz). Collectively, these observations suggest that the transition from the glassy state to the viscous state has already begun in the nanowire feature at the room temperature. This is further supported by the temperature dependence of the storage modulus (Figure 16 (b)) wherein the sensitivity of storage modulus versus temperature is higher at higher frequencies, as is observed in the transition region in Figure 18.

The dynamic tests performed here suggests that the nanowires are more viscous than glassy at the room temperature. This is indicative of a polymer with a low degree of cross-linking. This expectation is consistent with past work wherein the degree of conversion (i.e., the extent of cross-linking) in microstructures printed by TPL was observed to lie in the range of 20-40%[47]. It is expected that a glassy polymer would be generated with higher degrees of cross-linking such as those obtained at a higher writing dosage. In addition, glassy behavior is expected at temperatures lower than the room temperature. A more exhaustive study over several different writing conditions and over a larger temperature range would be required to verify these hypotheses. Previous work has showed a size effect on static material properties of the TPL polymer using DIC [32], and this work shows that this MEMS architecture meets the functional requirements necessary to further probe viscoelastic properties. Nevertheless, the work presented here demonstrates that the nanowire fabricated by TPL under the current writing conditions behaves as a viscoelastic material wherein the transition from glassy to viscous behavior has already set in at the room temperature.

V. Conclusion

We have developed a MEMS-based DMA that can be integrated with the TPL process and overcomes sample handling challenges. *This has enabled us to evaluate the* scale dependent dynamic mechanical properties and tensile loading of *nanowires fabricated by TPL*. The two-sensor design electrically measures stress and strain allowing high frequency sampling of structure deformations and stresses at the sensor surface or across the height of the 3D structure. Dynamic mechanical analysis of the TPL *nanowire demonstrated that the feature behaves as a viscoelastic material wherein the transition from glassy to viscous behavior has already begun at the room temperature*.

Acknowledgments

This work was performed under the auspices of the U.S. Department of Energy by Lawrence Livermore National Laboratory under Contract DE-AC52-07NA27344 and by the University of Texas at Austin under subcontracts. Funding was available from LLNL's LDRD project 16-ERD-047. LLNL-JRNL-800262

We thank Steve Hunter, Marianne Ammendolia, and James Oakdale of Lawrence Livermore National Laboratory and Donghwan Kim of University of Texas at Austin for helpful discussions and guidance.

The work was partly done at the Texas Nanofabrication Facility supported by NSF grant NNCI-1542159.

References

[1] L. R. Meza, S. Das, and J. R. Greer, "Strong, lightweight, and recoverable three-dimensional ceramic nanolattices," *Science (80-.).*, vol. 345, no. 6202, pp. 1322–1326, 2014.

[2] L. R. Meza, A. J. Zelhofer, N. Clarke, A. J. Mateos, D. M. Kochmann, and J. R. Greer, "Resilient 3D hierarchical architected metamaterials," *Proc. Natl. Acad. Sci. U. S. A.*, vol. 112, no. 37, pp. 11502–11507, 2015.

[3] T. Zhu and J. Li, "Ultra-strength materials," *Prog. Mater. Sci.*, vol. 55, no. 7, pp. 710–757, 2010.

[4] J. S. Juan, M. L. Nó, and C. A. Schuh, "Nanoscale shape-memory alloys for ultrahigh mechanical damping," *Nat. Nanotechnol.*, vol. 4, no. 7, pp. 415–419, 2009.

[5] K. P. Menard, *Dynamic Mechanical Analysis A Practical Introduction*, 1st ed. Boca Raton: CRC Press LLC, 1999.

[6] L. J. Jiang, J. H. Campbell, Y. F. Lu, T. Bernat, and N. Petta, "Direct writing target structures by two-photon polymerization," *Fusion Sci. Technol.*, vol. 70, no. 2, pp. 295–309, 2016.

[7] M. Deubel, G. von Freymann, M. Wegener, S. Pereira, K. Busch, and C. M. Soukoulis, "Direct laser writing of three-dimensional photonic-crystal templates for telecommunications," *Nat. Mater.*, vol. 3, no. 7, pp. 444–447, 2004.

[8] J. Bauer *et al.*, "Push-to-pull tensile testing of ultra-strong nanoscale ceramic-polymer composites made by additive manufacturing," *Extrem. Mech. Lett.*, vol. 3, pp. 105–112, 2015.

[9] J. Bauer, a. Schroer, R. Schwaiger, and O. Kraft, "Approaching theoretical strength in glassy carbon nanolattices," *Nat. Mater.*, vol. 15, no. 4, pp. 438–443, 2016.

[10] J. S. Oakdale *et al.*, "Direct Laser Writing of Low-Density Interdigitated Foams for Plasma Drive Shaping," *Adv. Funct. Mater.*, vol. 27, no. 43, p. 1702425, 2017.

[11] M. M. Stevens and J. H. George, "Exploring and Engineering the Cell Surface Interface," *Science (80-.).*, vol. 310, pp. 1135–1138, 2005.

[12] S. J. Zhang *et al.*, "Controlling Young's modulus of polymerized structures fabricated by direct laser writing," *Appl. Phys. A Mater. Sci. Process.*, vol. 118, no. 2, pp. 437–441, 2014.

[13] S. K. Saha *et al.*, "Radiopaque Resists for Two-Photon Lithography to Enable Submicron 3D Imaging of Polymer Parts via X-ray Computed Tomography," *ACS Appl. Mater. Interfaces*, vol. 10, no. 1, pp. 1164–1172, 2018.

[14] S. K. Saha, D. Wang, V. H. Nguyen, Y. Chang, J. S. Oakdale, and S.-C. Chen, "Scalable submicrometer additive manufacturing," *Science (80-.).*, vol. 366, no. 6461, pp. 105–109, 2019.

[15] J. Ye, "An indentation technique for nanoscale dynamic viscoelastic measurements at elevated temperature," *Jpn. J. Appl. Phys.*, vol. 51, no. 8 PART 4, pp. 0–7, 2012.

[16] P. M. Johnson and C. M. Stafford, "Surface indentation arrays for high-throughput analysis of viscoelastic material properties," *Rev. Sci. Instrum.*, vol. 80, no. 10, 2009.

[17] L. J. Jiang *et al.*, "Two-photon polymerization: investigation of chemical and mechanical properties of resins using Raman microspectroscopy.," *Opt. Lett.*, vol. 39, no. 10, pp. 3034–7, 2014.

[18] K. Cicha, T. Koch, J. Torgersen, Z. Li, R. Liska, and J. Stampfl, "Young's modulus measurement of two-photon polymerized micro-cantilevers by using nanoindentation equipment," *J. Appl. Phys.*, vol. 112, no. 9, 2012.

[19] S. Krödel, L. Li, A. Constantinescu, and C. Daraio, "Stress relaxation in polymeric microlattice materials," *Mater. Des.*, vol. 130, no. April, pp. 433–441, Sep. 2017.

[20] FemtoTools_AG, "FT-NMT04 Nanomechanical Testing System Product Brochure."

[21] P. A. Yuya, D. C. Hurley, and J. A. Turner, "Contact-resonance atomic force microscopy for viscoelasticity," *J. Appl. Phys.*, vol. 104, no. 7, 2008.

[22] B. Pant, B. L. Allen, T. Zhu, K. Gall, and O. N. Pierron, "A versatile microelectromechanical system for nanomechanical testing," *Appl. Phys. Lett.*, vol. 98, no. 5, pp. 5–8, 2011.

[23] E. Hosseinian and O. N. Pierron, "Quantitative in situ TEM tensile fatigue testing on nanocrystalline metallic ultrathin films," *Nanoscale*, vol. 5, no. 24, pp. 12532–12541, 2013.

[24] H. D. Espinosa, Y. Zhu, and N. Moldovan, "Design and operation of a MEMS-based material testing system for in-situ electron microscopy testing of nanostructures," *J. Microelectromech. S.*, vol. 16, no. 5, p. 1231, 2007.

[25] Z. Yong, L. Xinyu, R. Changhai, Z. Yan Liang, D. Lixin, and S. Yu, "Piezoresistivity Characterization of Synthetic Silicon Nanowires Using a MEMS Device," *J. Microelectromechanical Syst.*, vol. 20, no. 4, pp. 959–967, 2011.

[26] D. Zhang, W. Drissen, J.-M. Breguet, R. Clavel, and J. Michler, "A high-sensitivity and quasi-linear capacitive sensor for nanomechanical testing applications," *J. Micromech. Microeng. J. Micromech. Microeng*, vol. 19, no. 19, pp. 75003–10, 2009.

[27] T. Tsuchiya, Y. Ura, K. Sugano, and O. Tabata, "Electrostatic Tensile Testing Device With Nanonewton and Nanometer Resolution and Its Application to Nanowire Testing," *J. Microelectromechanical Syst.*, vol. 21, no. 3, pp. 523–529, Jun. 2012.

[28] M. Naraghi, T. Ozkan, I. Chasiotis, S. S. Hazra, and M. P. De Boer, "MEMS platform for on-chip nanomechanical experiments with strong and highly ductile nanofibers," *J. Micromechanics Microengineering*, vol. 20, no. 12, p. 125022, 2010.

[29] R. K. Jayne, T. J. Stark, J. B. Reeves, D. J. Bishop, and A. E. White, "Dynamic Actuation of Soft 3D Micromechanical Structures Using Micro-Electromechanical Systems (MEMSs)," *Adv. Mater. Technol.*, vol. 1700293, pp. 1–6, 2018.

[30] Q. Qin *et al.*, "Recoverable plasticity in penta-twinned metallic nanowires governed by dislocation nucleation and retraction," *Nat. Commun.*, 2015.

[31] M. Naraghi, L. Chasiotis, H. Kahn, Y. Wen, and Y. Dzenis, "Novel method for mechanical characterization of polymeric nanofibers," 2007.

[32] I. S. Ladner, M. A. Cullinan, and S. K. Saha, "Tensile properties of polymer nanowires fabricated via two-photon lithography," *RSC Adv.*, vol. 9, pp. 28808–28813, 2019.

[33] M. Naraghi, I. Chasiotis, H. Kahn, Y. Wen, Y. Dzenis, and H. Kahn, "Mechanical deformation and failure of electrospun polyacrylonitrile nanofibers as a function of strain rate Mechanical deformation and failure of electrospun polyacrylonitrile nanofibers as a function of strain rate," vol. 151901, no. 2007, pp. 88–91, 2014.

[34] R. Hickey, D. Sameoto, T. Hubbard, and M. Kujath,

"Time and frequency response of two-arm micromachined thermal actuators," *J. Micromechanics Microengineering*, vol. 13, no. 1, pp. 40–46, Jan. 2003.

[35] Z. Yapu, "Stiction and anti-stiction in MEMS and NEMS," *Acta Mech. Sin.*, vol. 19, no. l, pp. 1–10, 2003.

[36] C. H. Mastrangelo and C. H. Hsu, "Mechanical stability and adhesion of microstructures under capillary forces. II. Experiments," *J. Microelectromechanical Syst.*, vol. 2, no. 1, pp. 44–55, 1993.

[37] O. Raccurt, F. Tardif, F. A. D'Avitaya, and T. Vareine, "Influence of liquid surface tension on stiction of SOI MEMS," *J. Micromechanics Microengineering*, vol. 14, no. 7, pp. 1083–1090, 2004.

[38] R. L. Alley, G. J. Cuan, R. T. Howe, and K. Komvopoulos, "The effect of release-etch processing on surface microstructure stiction." pp. 202–207, 1992.

[39] O. Raccurt, F. Tardif, F. A. d\textquotesingleAvitaya, and T. Vareine, "Influence of liquid surface tension on stiction of {SOI} {MEMS}," *J. Micromechanics Microengineering*, vol. 14, no. 7, pp. 1083–1090, Jun. 2004.

[40] Nanoscribe, "RESIN PROPERTIES APPLICATIONS Properties IP-Q IP-S IP-Dip IP-G 780 IP-L 780 Cell Scaffolds," pp. 2–3.

[41] M. Ehmann, P. Ruther, M. Von Arx, and O. Paul, "Operation and short-term drift of polysilicon-heated CMOS microstructures at temperatures up to 1200 K," *J. Micromechanics Microengineering*, vol. 11, no. 4, pp. 397–401, 2001.

[42] Y. Zhu, A. Corigliano, and H. D. Espinosa, "A thermal actuator for nanoscale in situ microscopy testing : design and characterization," 2006.

[43] *Chapter 2 PolyMUMPs Design Guidelines and Rules*, Rev. 13.0., vol. 1. .

[44] S. K. S. Ian S. Ladner, Michael A. Cullinan, "Processing-dependent tensile behavior of polymer nanowires fabricated via two-photon lithography," *RSC Adv. (under Rev.*, 2019.

[45] I. S. Ladner, "Mechanical Characterization of Two-Photon Polymerization Submicron Features," (Doctoral Disseration). University of Texas at Austin, 2018.

[46] K. P. Menard, *Dynamic Mechanical Analysis: A Practical Application*. 2007.

[47] J. S. Oakdale, J. Ye, W. L. Smith, and J. Biener, "Post-print UV curing method for improving the mechanical properties of prototypes derived from two-photon lithography," *Opt. Express*, vol. 24, no. 24, p. 27077, 2016.